

## A Virtual Pivot Point MEMS Actuator with Externally Mounted Mirror: Design, Fabrication and Characterization

<sup>1,2</sup>T. M. Fahim AMIN, <sup>2</sup>M. Q. HUDA, <sup>3</sup>J. TULIP, <sup>1</sup>Wolfgang JÄGER

<sup>1</sup>Dept. of Chemistry, University of Alberta, Edmonton, AB T6G 2G2, Canada

<sup>2</sup>Dept. of Electrical and Computer Eng., University of Alberta, Edmonton, AB T6G 2G2, Canada

<sup>3</sup>Boreal Laser Inc., Edmonton, AB T5L 2H7, Canada

<sup>1</sup>Tel.: +1 780 4925020, fax: +1 780 4928231

E-mail: [tmfahim@ualberta.ca](mailto:tmfahim@ualberta.ca), [wolfgang.jaeger@ualberta.ca](mailto:wolfgang.jaeger@ualberta.ca)

*Received: 20 October 2014 /Accepted: 28 November 2014 /Published: 31 December 2014*

**Abstract:** In this paper, the design, fabrication, and characterization of a virtual pivot point micro electromechanical systems (MEMS) electrostatic actuator with externally mounted mirror is presented. The point of rotation of the movable arm of the actuator is distant from the physical actuator. This is a requirement for certain applications, such as an external cavity laser in Littman configuration. A maximum rotational radius of 5 mm from the virtual pivot point was achieved. A detailed analytical analysis for the displacement of the structure is presented. The dynamic characterization of the device with a finite element analysis simulation shows that the resonance frequency of the in-plane rotational mode is well separated from that of the out-of-plane bending mode, confirming high in-plane stability. The devices were fabricated on a silicon-on-insulator wafer with device layer thickness of 100  $\mu\text{m}$ . Thin mirrors were fabricated by dicing a 100  $\mu\text{m}$  thick silicon wafer. A resonance frequency of about  $5.9 \times 10^2$  Hz for the maximum sized mounted mirror (1.7 mm  $\times$  100  $\mu\text{m}$   $\times$  1.0 mm) was determined by optical characterization. *Copyright © 2014 IFSA Publishing, S. L.*

**Keywords:** MEMS, Optical MEMS, External cavity laser, Tunable laser, Micromirror, Virtual pivot.

### 1. Introduction

MEMS mirrors have become common in miniature structures and are used in many optical applications. While some of these applications are already at the commercial stage, such as projection displays, optical scanners, and optical switching [1-3], significant research activities are currently directed towards the use of MEMS mirrors in other applications, including external cavity lasers (ECLs) [4], adaptive optics [5], optical tomography [6-7], and galvanometric scanners [8]. In many cases, the anticipated application dictates the size of the MEMS mirror and its plane of movement. Micro-sized

mirrors favor high frequency operation which is suitable in switching and projection display operation. Many other applications demand larger mirror sizes to achieve sufficient light reflection for its operation [5-9]. Most of the large MEMS mirrors reported in the literature are fabricated on top of the silicon plane and provide out-of-plane movement through a tilt motion. However, some applications, for example mirror tuning of an ECL, demand in-plane lateral movement of the MEMS component. MEMS devices can be fabricated for lateral operation using bulk micromachining processes of silicon-on-insulator (SOI) wafers and the sidewall can in principle be used as mirror surface [10]. However,

the size of the mirror is then limited by the thickness of the device layer and the maximum achievable depth for uniform etching. The surface quality of the etched sidewall is also an issue for applications that require minimum light scattering. One way to overcome this issue is to mount an external mirror onto a MEMS actuator [11].

In this paper, we present the design and fabrication process of a virtual pivot point (VPP) actuator with the provision of mounting external optical components [12]. The VPP actuator has a radius of up to 5 mm and a physical clearance of 3 mm from the pivot point location. We also describe an efficient process for mounting an externally fabricated mirror onto the MEMS actuator.

## 2. Device Design and Operation

The VPP design of a rotary comb actuator implements a pivot point that is remote from the physical actuator [10]. It thus allows an optical beam to pass between the physical actuator and the pivot point for in-plane applications and also provides space for additional optical components. For example, continuous wavelength tuning of an ECL in both Littrow and Littman configuration is possible through rotation of the tuning element (mirror/grating) about a pivot point [13]. The VPP actuator described here is specifically designed for operation in a Littman configured ECL, in which optical beam and rotation axis intersect. Nevertheless, the actuator can equally be used in Littrow configured ECLs and other optical applications which require large mirrors. The device has a maximum radius of 5 mm and a physical clearance of 3 mm from the pivot point. A schematic diagram of the designed VPP rotary comb electrostatic actuator is shown in Fig. 1.

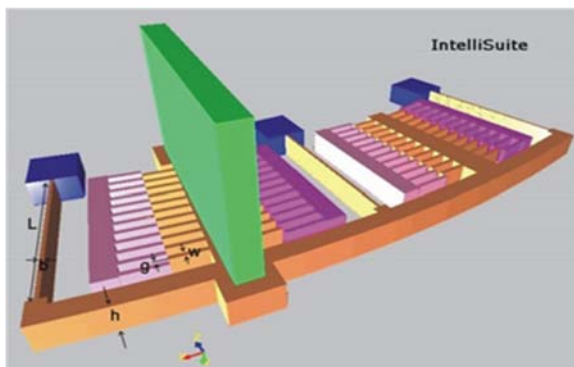


**Fig. 1.** Schematic diagram of a VPP actuator with mounted external mirror.

Four sets of rotary comb drive pairs were used in the design to generate sufficient electrostatic force to achieve the desired rotation angle.

The comb drives are connected through rigid arc-shaped trusses at the top and the entire movable

structure is anchored through three beams. Two trusses from which the moving comb fingers extend are positioned along the radial direction from the VPP. They were designed with high stiffness to carry the mirror. In our design, two of the four sets of comb drives generate force to rotate the actuator in one direction (for example, the first and third comb drives for clockwise rotation) and the other two actuate during rotation in the opposite direction. The electrostatic force is balanced by the restoring spring force provided by the three anchored beams according to Hooke's law. See Table 1 for design parameters.

**Table 1.** Design parameters of the fabricated actuator.

	Length/Arc size	Width	Height
<b>Beam Dimension</b>	1500 $\mu\text{m}$	9 $\mu\text{m}$	100 $\mu\text{m}$
<b>Comb Finger</b>	1.8 deg	7.4 $\mu\text{m}$	100 $\mu\text{m}$
<b>Mirror Size</b>	1.7 mm	100 $\mu\text{m}$	1 mm
<b>Maximum Radius from Pivot Point</b>	5010 $\mu\text{m}$		

In the following, we describe an analytical model for the designed actuator. For a larger truss length with a smaller arc length of comb fingers, a parallel plate configuration can be assumed. The electrostatic force generated by a set of  $n$  rotary comb fingers with an applied voltage  $V$  can then be expressed by:

$$F = \frac{nehV^2}{g}, \quad (1)$$

where  $h$  is the finger thickness,  $g$  is the gap between the fingers,  $\epsilon$  is permittivity of air and  $n$  is the number of moving comb fingers. The design of the VPP actuator can be represented by an approximate straight model as shown in Fig. 2(a). In the approximate model, the force generated by the comb fingers is given by an equivalent point force at the middle of comb drive. The approximate model can be further simplified by removing the folded truss, as shown in Fig. 2(b). The effect of the force on the two folded truss is modeled by an equivalent moment and force applied at the top of the truss where the equivalent moment is given by  $M=FL_F$ . The simplified model in Fig. 2(b) resembles a portal frame structure [14]. As the simplified model is still a statically indeterminate structure, we used the force method [15] to solve for the unknown redundant forces and moments of the structure. In the force method, the degree of indeterminacy of the structure,  $i$ , is first determined and then the  $i$  unknown redundant forces or moments are selected. The redundants are selected in such a way that when they are removed, the structure become statically determinate and stable.

Removing the restraints, which correspond to all the redundants from the indeterminate structure, gives the primary (determinate) structure, where the

external load is also present (Fig. 3 for our VPP model).

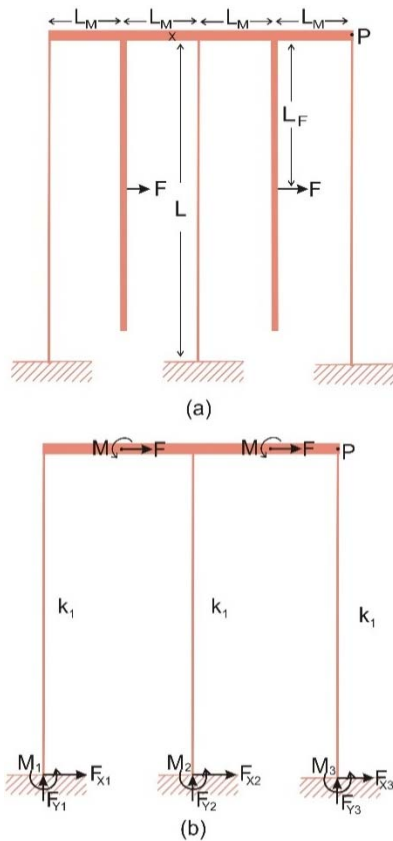


**Fig. 2.** Modeling of the virtual pivot structure; (a) an approximate model; (b) simplified model after removing the folded truss.

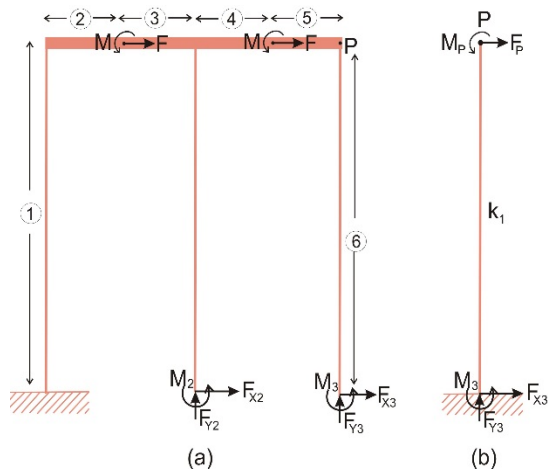


**Fig. 3.** (a) Primary structure for the force method of calculation. The restraints, which correspond to the selected redundants ( $M_2, F_{x2}, F_{y2}, M_3, F_{x3}, F_{y3}$ ), are removed. The sections labelled by numbers are considered individual sections in the calculation; (b) an equivalent displacement model using a single beam structure.

Removing the external load from the primary structure and assigning a unit value of force or moment to a single redundant leads to further

determinate structures. Using the principle of superposition, the statically indeterminate structure is equal to this series of statically determinate structures. Finally, compatibility equations are formed to solve for displacement or rotation at each section of the structure where there is a redundant force or moment. These equations are expressed in terms of the unknown redundants and their corresponding flexibility coefficients obtained from unit loads or unit couple moments that are collinear with the redundant forces or moments. The compatibility equations for our structure, which has a degree of indeterminacy of 6, can be expressed as [15]:

$$\Delta + fR = 0, \quad (2)$$

where  $\Delta$  is the displacement matrix,  $f$  is the flexibility matrix and  $R$  is the redundants matrix of the structure. For  $i$  redundants, the flexibility matrix is an  $i \times i$  matrix, and  $\Delta$  and  $R$  are column matrices with  $i$  elements.

The elements of the matrix  $\Delta$  are given by:

$$\Delta_i = \sum_{m=1}^{m=m} \int \frac{M_{om} M_{im}}{EI}, \quad (3)$$

where  $M_{om}$  and  $M_{im}$  are the bending moments on each section of the structure for an external load and a unit load of redundant  $R_i$  respectively. The individual elements of the flexibility matrix are given by:

$$f_{ii} = \sum_{m=1}^{m=m} \int \frac{M_{im} M_{im}}{EI}, \quad (4)$$

$$f_{ij} = f_{ji} = \sum_{m=1}^{m=m} \int \frac{M_{im} M_{jm}}{EI}, \quad (5)$$

where  $M_{im}$  and  $M_{jm}$  represent the bending moments in section  $m$  resulting from the unit loads of redundants  $R_i$  and  $R_j$ , respectively. Since all three beams have the same dimensions and are connected through a rigid truss, the structure will have the same lateral displacement on all the points which are at the same distance from the anchor point. Upon determining all the redundant forces and moments, the structure can be represented by a free body diagram of a single beam (the displacement model) with equivalent force and moment at its tip, as shown in Fig 3(b). The force,  $F$ , in the displacement model is the reaction force at the base of the third beam,  $F_P = -F_{x3}$  and the equivalent moment  $M_P = M_3 - FL$ , where  $L$  is the length of the beam. The displacement can then be determined by using the displacement formula of a cantilever beam for an applied force of  $F_P$  and a moment of  $M_P$ . The moment works in the opposite direction of the force and the total displacement,  $x$ , at the tip,  $P$ , is given by:

$$x = \frac{F_p L^3}{3EI} - \frac{M_p L^2}{2EI}, \quad (6)$$

where  $E$  is the Young's modulus of silicon and  $I$  is the area moment of inertia of the beam.

We also simulated the VPP actuator using the MEMS simulation software Intellisuite [16] to obtain the actual displacement as a function of applied voltage. Fig. 4 shows a comparison of the calculated maximum displacement of the virtual pivot point model with the simulation results.

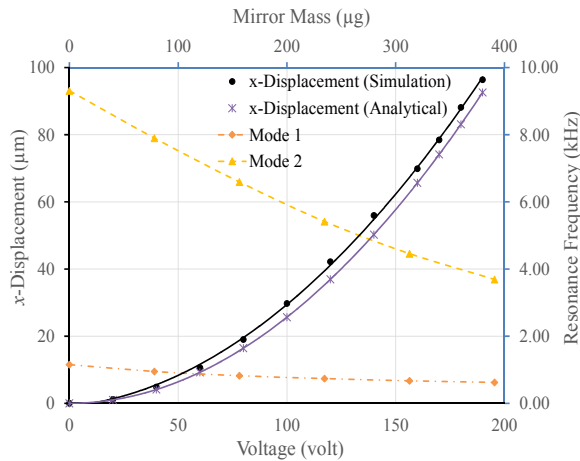


**Fig. 4.** Displacement at the topmost point of the actuator along the  $x$ -coordinate as function of voltage (solid lines) and variation of the resonance frequencies of the two lowest modes of the actuator (dashed lines) with mirror mass.

The generated force from the comb drive is considered at a distance of  $797.3 \mu\text{m}$  from the topmost truss during the calculation. As shown in the graph, the simulated and the calculated displacements for the virtual pivot model are quite close to each other. The simulated displacement for the actual device is slightly larger than the calculated displacements of the virtual pivot point model. A number of factors may contribute to this larger displacement. The maximum displacement is found at the end of the connecting truss in the simulation whereas the maximum displacement is calculated at the tip of cantilever beam from the analytical model. The omission of the width of the truss during the analytical calculation reduces the analytical displacement slightly. Other factors that can contribute to the deviation are, for example, assumption of a straight connecting truss in the analytical model while the actual truss is curved and neglecting the fringe field effect in the analytical force calculation.

The behaviour of the structure was also simulated to determine the effect of mounting an external mirror. The resonance frequency of structure decreases with increase of mirror mass, as anticipated. The two dashed traces in Fig. 4 show the change of resonance frequency with mirror mass.

Mode 1 represents the in-plane vibration and Mode 2 the out-of-plane vibration of the structure. It is apparent that the frequency of the out-of-plane vibration frequency is much higher than the in-plane frequency, which confirms the in-plane stability of structure.

### 3. Device Fabrication

The actual device has dimensions of  $2 \text{ mm} \times 2 \text{ mm}$  and was fabricated on a  $4 \text{ mm} \times 5 \text{ mm}$  chip. An SOI wafer with device layer thickness of  $100 \mu\text{m}$ , buried oxide layer of  $2 \mu\text{m}$ , and substrate layer thickness of  $300 \mu\text{m}$ , as depicted in Fig. 5(a), was used for the device fabrication. Bulk micro-machining was performed from both sides of the wafer and involved two level masking. The mask sets were designed with largely spaced open areas around the devices to facilitate easier mounting of the external mirror and easier alignment of the light beam onto the mirror. This made the fabrication process challenging as the wafer became structurally weak due to the removal of bulk silicon from the handle layer. We developed a fabrication process that involved patterning of both sides of the wafer before any deep etch, as shown in Fig. 5(a) – (j).

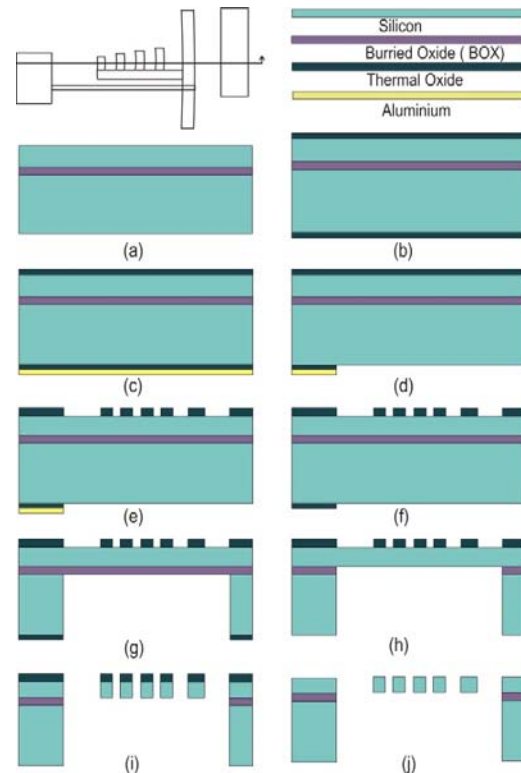


**Fig. 5.** Step-by-step illustration of the actuator fabrication; (a) SOI wafer; (b) thermally grown oxide on both sides; (c) Al sputtering on the back side; (d) patterning of Al, etching of Al layer and oxide layer; (e) patterning of front layer; (f) removal of Al from the back; (g) removal of Si using DRIE; (h) removal of buried oxide; (i) etching of Si device layer and (j) removal of residual thermal oxide from the top.

At first, a thermal oxide layer was grown on both sides of the wafer as masking layer to utilize the higher etching selectivity of SiO<sub>2</sub> over Si (100:1). Aluminum (Al) was then deposited onto the backside of the wafer with a sputtering process to assist the alignment of front and back patterns. The Al layer on the backside was then patterned by photolithography using HPR 506 photoresist followed by etching with commercial Al etchant (16:1:1:2 solution of phosphoric acid, nitric acid, acetic acid, and water). The pattern was then transferred onto the oxide layer by etching the SiO<sub>2</sub> layer using a reactive ion etch (RIE) process.

The same process, except the Al patterning steps, was used to pattern the front side SiO<sub>2</sub> layer. The backside Al layer, opaque to infrared light, assisted the alignment process without any deep etch. After patterning of both sides, the wafer was diced into individual dies for further processing. Batches of 10 to 20 dies were then mounted on a carrier wafer and deep etching of Si down to the buried oxide layer was performed from the back side. An optimized deep RIE (DRIE) recipe was used in an STS inductively coupled plasma (ICP) machine to achieve good vertical feature profiles. We used the Bosch plasma etching process [17, 15], which consists of two alternating steps, i.e. etching and passivation. A stronger passivation step tends to produce a positive profile, but increases grass at the bottom of the feature and reduces the etch rate. On the other hand, a stronger etching step increases the etch rate and reduces grass, but makes the profile negative. Optimization was achieved by experimenting with the plasma process parameters such as etch/passivation cycle time, gas flow, ICP coil power, chamber pressure, and electromagnet settings. After DRIE, we removed the buried oxide layer using RIE from the back side.

The dies were then un-mounted from the carrier wafer and thoroughly cleaned. We mounted them again on a carrier wafer and performed DRIE from the front side to transfer the pattern onto the Si device layer from the oxide mask. The actuators were released upon completion of this stage. The residual oxide mask layer was then removed using RIE and a thin gold layer was deposited using a sputtering process for better electrical contact. An SEM image of a fabricated device is shown in Fig. 6.

#### 4. External Mirror Mounting

Two contact pads were inscribed at the top and bottom of the right truss in our design to facilitate mounting of an external mirror, as shown in Fig. 6. Si mirrors were fabricated from a commercially available 100  $\mu\text{m}$  thin Si wafer, polished on both sides. The wafer was first diced into different suitable mirror sizes using a Disco DAD 321 dicing saw. Thin layers of chromium (Cr~15 nm) and gold (Au ~50 nm) were then deposited onto the individual

mirror pieces through sputtering. Gold was used on the mirror surface to increase its reflectivity. We developed an efficient method to mount the external mirror onto the MEMS device to minimize problems associated with manual handling of the thin Si mirrors.

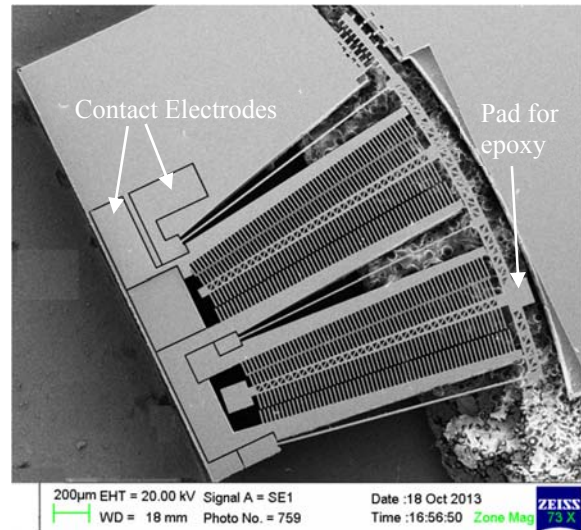


Fig. 6. An SEM image of a VPP actuator.

A die bonding system consisting of a microscope, a moving stage, a heater, and a vacuum tip, was used to develop the mirror mounting method. Epotek H20E Silver filled epoxy [18] was used as the bonding material between the MEMS device and the mirror. The epoxy cures within 15 minutes at 120  $^{\circ}\text{C}$ . The mirror mounting setup is shown in Fig. 7.

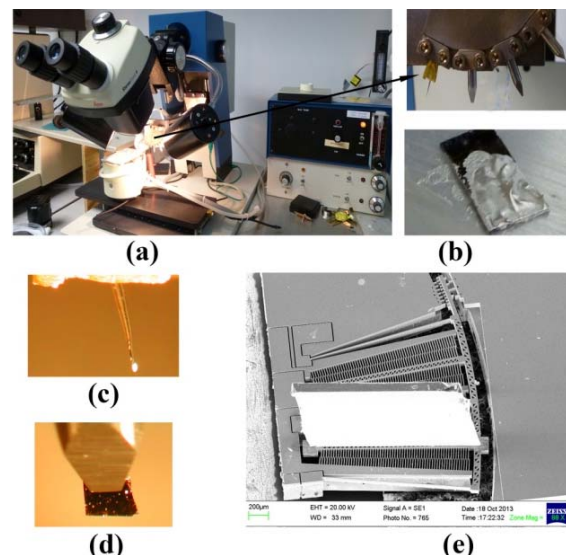
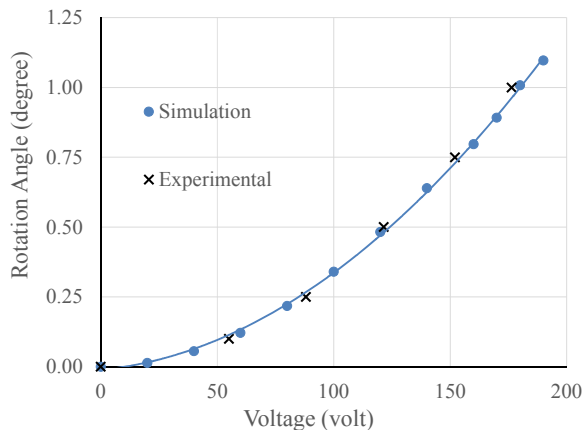


Fig. 7. Mirror mounting setup and mounting process; (a) the die bonding machine used for mirror mounting (the top right picture shows a close-up of the vacuum tips); (b) silver epoxy mixture; (c) a drop of epoxy at the tip of the needle; (d) a mirror picked up by the vacuum tip; and (e) an SEM image of an actuator with mounted mirror.

The die bonding system (Fig. 7 (a)) has different types of vacuum tips just above the movable stage. An enlarged view of the tip assembly is shown by the arrow. A needle was used to pick up a drop of epoxy and the vacuum tip (next to it), which has a slot to keep the mirror straight, was used to pick up the mirror piece and to release it. Fig. 7 (b)-(c) shows the epoxy mixture and a tiny dot of epoxy on the needle. A mirror picked up vertically by the vacuum tip is shown in Fig. 7 (d). The mirror piece was aligned with the mirror holder on the MEMS actuator and released onto it with the help of the microscope and moving arm. Fig. 7 (e) shows an SEM image of an actuator with mounted external mirror.

## 5. Results and Discussion

A vernier scale was inscribed into each chip during the mask design to facilitate measurement of the rotation angle on a wafer probing station. Measured and simulated rotation angles are in excellent agreement (see Fig. 8). We also achieved symmetrical displacements in clockwise and counter-clockwise directions.



**Fig. 8.** Measured and simulated rotation angles of the actuator as function of applied voltage.

After mounting the mirror, we characterized the device using an optical technique. A schematic diagram of the optical testing setup is shown in Fig. 9. The beam of a red laser pointer (630-680 nm, maximum output <5 mW) was aimed at the mounted mirror and the reflected beam was detected using a photodetector (Alphas, wavelength range 320-110 nm, detector area 0.5 mm<sup>2</sup>). The photodetector output was recorded with a digital oscilloscope. The device was actuated with a square wave driving voltage and the vibration after the sudden actuation was captured by recording the photodetector output. Fig. 10 shows a captured photodetector signal for an actuation voltage of 120 V at a frequency of 1 Hz. Only a 10 ms section near the up-going voltage step is shown in the figure.

Increasing the frequency increases the vibration at the actuated position because of the increased speed of the actuator.

Analysis of the oscilloscope traces resulted in a lowest vibration frequency of  $5.9 \times 10^2$  Hz for a maximum mounted mirror size of  $1.7 \text{ mm} \times 100 \mu\text{m} \times 1 \text{ mm}$ . This is very close to frequency of  $6.2 \times 10^2$  Hz from the simulation. The slight deviation can be attributed to uneven beam widths of the actuator produced in the DRIE process.

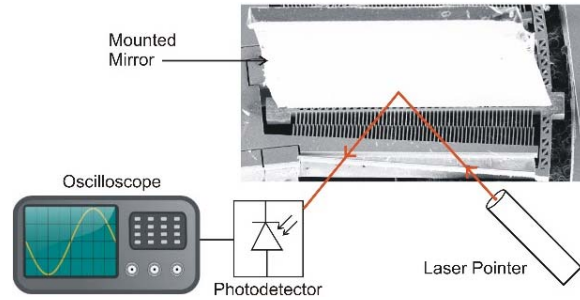


**Fig. 9.** Schematic diagram of the optical testing setup.

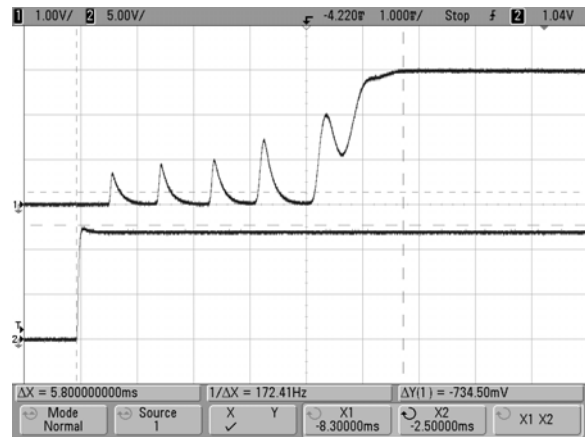


**Fig. 10.** Captured photodetector output for a square wave of 120 V, 1 Hz.

## 6. Conclusions

In this paper, we present the design, fabrication, and characterization of a VPP comb drive actuator with the provision of mounting optical components. A detailed analytical analysis of the designed structure was carried out and the analytical results compare well with those from a numerical simulation and with the experimental results. The actuator provides a tip displacement of about 96  $\mu\text{m}$  (equivalent to 1.1°) for a voltage of 190 V. The dynamic characterization of the actuator confirms the in-plane stability of the devices with mounted external mirror. A procedure for mounting optical components was developed. The resonance frequency of the device with mounted mirror of size  $1.7 \text{ mm} \times 100 \mu\text{m} \times 1 \text{ mm}$  was

determined to be  $5.9 \times 10^2$  Hz using an optical characterization method.

## Acknowledgements

We thank Dr. G. McKinnon and Dr. N. Ponnampalam, Norcada Inc., for discussions and support, and for help with the development of the mirror mounting technique. We are also grateful to Mohommad Mamun from the Department of Civil Engineering at the University of Alberta for his help with the structural analysis. This work was supported by the nanoWorks Program of Alberta Innovates Technology Futures and by the Natural Sciences and Engineering Research Council of Canada.

## References

- [1]. P. F. van Kessel, L. J. Hornbeck, R. E. Meier, M. R. Douglass, A MEMS-based projection display, in *Proceedings of the IEEE*, Vol. 86, 1998, pp. 1687-1704.
- [2]. N. Asada, M. Takeuchi, V. Vaganov, N. Belov, I. Sluchak, Silicon micro-optical scanner, *Sensors and Actuators A: Physical*, Vol. 83, 2000, pp. 284-290.
- [3]. P. De Dobbelaere, K. Falta, S. Gloeckner, S. Patra, Digital MEMS for optical switching, *Communications Magazine, IEEE*, Vol. 40, 2002, pp. 88-95.
- [4]. A. Q. Liu, X. M. Zhang, A review of MEMS external-cavity tunable lasers, *J. Micromech Microengineering*, Vol. 17, 2007, pp. R1-R13.
- [5]. P.-Y. Lin, H.-T. Hsieh, G.-D. J. Su, Design and fabrication of a large-stroke MEMS deformable mirror for wavefront control, *Journal of Optics*, Vol. 13, 2011, pp. 055404-055412.
- [6]. Y. Pan, H. Xie, G. K. Fedder, Endoscopic optical coherence tomography based on a microelectromechanical mirror, *Optics Letter*, Vol. 26, 2001, pp. 1966-1968.
- [7]. B. Qi, A. P. Himmer, L. M. Gordon, X. D. V. Yang, L. D. Dickensheets, I. A. Vitkin, Dynamic focus control in high-speed optical coherence tomography based on a microelectromechanical mirror, *Optical Communication*, Vol. 232, 2004, pp. 123-128.
- [8]. L. O. S. Ferreira, S. Moehlecke, A silicon micromechanical galvanometric scanner, *Sensors and Actuators A: Physical*, Vol. 73, 1999, pp. 252-260.
- [9]. T. Fujita, K. Maenaka, Y. Takayama, Dual-axis MEMS mirror for large deflection-angle using SU-8 soft torsion beam, *Sensors and Actuators A: Physical*, Vol. 121, 2005, pp. 16-21.
- [10]. T. Amin, M. Huda, Y. Ning, G. McKinnon, J. Tulip, W. Jäger, A virtual pivot point MEMS rotary comb actuator for tunable laser applications, in *SPIE Proceeding*, 8490, 2012, 84900D.
- [11]. J. D. Berger, Y. Zhang, J. D. Grade, H. Lee, S. Hrinya, H. Jerman, Widely tunable external cavity diode laser using a MEMS electrostatic rotary actuator, in *Proceeding 27<sup>th</sup> European Conference on Optical Communication (ECOC)*, 2001, pp. 198-199.
- [12]. T. M. F. Amin, M. Q. Huda, J. Tulip, W. Jäger, Virtual pivot point MEMS rotary comb actuator with externally mounted mirror for optical applications, in *Technical Proceeding of the NSTI-Nanotech'14*, Washington, D.C., USA, 2014, pp. 17-20.
- [13]. M. G. Littman, H. J. Metcalf, Spectrally narrow pulsed dye laser without beam expander, *Appl. Opt.*, Vol. 17, 1978, pp. 2224-2227.
- [14]. A. Kassimali, Structural Analysis, *Cengage Learning*, 2010.
- [15]. R. C. Hibbeler, K. Tan, B. Nolan, Structural Analysis, *Pearson Prentice Hall*, 2006.
- [16]. Intellisuite 8.2. (<http://www.intellisense.com/>).
- [17]. F. Laermer, A. Schilp, Method of Anisotropically Etching Silicon, *US 5501893 A*, 1996.
- [18]. Epotek (<http://www.epotek.com/>).

2014 Copyright ©, International Frequency Sensor Association (IFSA) Publishing, S. L. All rights reserved. (<http://www.sensorsportal.com>)

Promoted by IFSA

# Status of the MEMS Industry Report up to 2017

Report includes MEMS device markets, key players strategies, key industry changes and MEMS financial analysis. It also includes major MEMS manufacturing evolutions as well as an update on the "emerging" MEMS device markets.

Order online:

[http://www.sensorsportal.com/HTML/Status\\_of\\_MEMS\\_Industry.htm](http://www.sensorsportal.com/HTML/Status_of_MEMS_Industry.htm)